1
2
3

InSegtCone: Interactive Segmentation of crystalline Cones in compound eyes

4 **Abstract**

5

6 Understanding the diversity of eyes is crucial to unravel how different animals use vision to
7 interact with their respective environments. To date, comparative studies of eye anatomy are
8 scarce because they often involve time-consuming or inefficient methods. X-ray micro-
9 tomography is a promising high-throughput imaging technique that enables to reconstruct the
10 3D anatomy of eyes, but powerful tools are needed to perform fast conversions of anatomical
11 reconstructions into functional eye models. We developed a computing method named
12 *InSegtCone* to automatically segment the crystalline cones in the apposition compound eyes of
13 arthropods. Here, we describe the full auto-segmentation process, showcase its application to
14 three different insect compound eyes and evaluate its performance. The auto-segmentation
15 could successfully label the full individual shapes of 60%-80% of the crystalline cones, and is
16 about as accurate and 250 times faster than manual labelling of the individual cones. We
17 believe that *InSegtCone* can be an important tool for peer scientists to enable extensive
18 comparisons of the diversity of eyes and vision in arthropods.

19

20 **Authors and affiliations**

21

22 Pierre Tichit[1*], Tunhe Zhou[2*], Hans Martin Kjer[3], Vedrana Andersen Dahl[3], Anders Bjorholm
23 Dahl[3], and Emily Baird[1,4]

24

25 °Corresponding author at Lund University. E-mail address: pierre.tichit@biol.lu.se
26 [1]Department of Biology, Lund University, Lund 223 62, Sweden
27 [2]Stockholm University Brain Imaging Center, 114 18 Stockholm, Sweden
28 [3]Department of Applied Mathematics and Computer Science, Technical University of
29 Denmark, DK-2800 Kgs. Lyngby, Denmark
30 [4]Department of Zoology, Stockholm University, 114 18 Stockholm, Sweden
31 [*]These authors contributed equally to this work.

32

33 **Keywords**

34

35 X-ray microtomography, Arthropods, Compound eye, Crystalline cones, Segmentation, Image
36 analysis

37

38 **Introduction**

39

40 Arthropods comprise more than 80% of animals living on the planet (Roskov et al., 2000) but
41 little is known about the diversity of the visual systems in this phylum (Rosenthal et al. 2017).
42 Many arthropods make extensive use of visual information to perform essential behaviours,
43 such as locating suitable mates, finding food or avoiding predators (Cronin et al., 2014). To
44 better understand how these animals interact with their environment, it is therefore important
45 to carry out anatomical and functional investigations of the myriad of arthropod eyes.
46 Moreover, better understanding the eyes of arthropods will not only inform us about the visual
47 ecology of these species, but also about fundamental aspects of animal vision.
48   Most Arthropods have a pair of compound eyes consisting of repeated units called
49 ommatidia. An ommatidium typically consists of three elements: an external lens that forms a
50 regular facet visible on the external surface of the eye, a crystalline cone and a rhabdom (Land

51 and Nilsson, 2012). The light-sensitive rhabdom is the 'sensor' unit that collects light provided
52 by unique (in apposition compound eyes) or multiple (in superposition compound eyes)
53 transparent 'optics' unit – the lens and the crystalline cone. Each ommatidium samples light
54 from a small angular portion of the world that, once integrated, enables arthropods to generate
55 detailed and colourful images across the field of view (FOV) of the compound eye.
56   To be able to resolve an object in a given light regime, each portion of a compound eye
57 trades-off adequate spatial resolution and sufficient light capture, or optical sensitivity (Land,
58 1997). This is because spatial resolution is ultimately determined by the angular spacing of the
59 neighbouring ommatidia – the inter-ommatidial (IO) angle – such that a reduction in IO angle
60 increases resolution. On the contrary, optical sensitivity depends on the angular area over
61 which photons are captured; a bigger IO angle therefore leads to better sensitivity. The optical
62 properties of ommatidia thus typically vary across the topology of compound eyes to optimise
63 resolution and/or sensitivity in different parts of the FOV in a way that reflects the ecology of
64 the animal. For example, the frontal region of the eye of the male carpenter bee *Xylocopa*
65 *tenuiscapa* has enlarged ommatidia with small IO angle, which enhances both sensitivity and
66 resolution and probably is an adaptation for detecting and chasing mates (Somanathan et al.,
67 2017). Thus, anatomical comparisons of compound eyes across sexes, castes, life-stages,
68 populations or species, provide formidable opportunities to better understand the visual
69 ecology and behaviour of arthropods.
70   Exploring how the ecology of arthropods relates to their visual anatomy requires large-
71 scale and detailed analysis of eye structures, something that is challenging for two major
72 reasons. Firstly, it necessitates investigations into the inner anatomy of compound eyes,
73 because properties such as the elongation axes of crystalline cones and the diameters and
74 lengths of rhabdoms are needed for accurate calculations of optical sensitivity and IO angle
75 (Land, 1997). Furthermore, these properties must be measured in high-resolution across the
76 eye to obtain reliable topological information (Taylor et al., 2019a). Traditional methods to
77 study visual anatomy provide incomplete information and/or are too time consuming to enable
78 large-scale analyses. Imaging methods such as Transmission Electron Microscopy (TEM), a
79 technique that is typically used to measure rhabdom properties, are slow and produce coarse
80 topologies from only a few slices in each eye sample. The pseudopupil technique (Berry et al.,
81 2007), which measures the topology of IO angle, is relatively fast but requires live animals and
82 typically generates coarse resolution maps that do not include the full extent of the FOV (Taylor
83 et al., 2019a), sometimes filtering out precious fine-scale information (Bagheri et al., 2020).
84   How can we quickly obtain fine-scale topological data, both on the outside and the
85 inside of compound eyes that typically possess thousands of ommatidia? X-ray
86 microtomography (micro-CT) is a promising method to generate fast (a scan typically lasts
87 from a few minutes to a few hours) and accurate (with isotropic spatial resolution of a
88 micrometre or less) 3D models of an eye (Baird and Taylor, 2017). This method has the
89 advantage of keeping the eye geometry intact, unlike 2D methods that inherently lose part of
90 the geometrical information through the physical sectioning process. In a recent study, Taylor
91 et al. (2019a) used micro-CT to obtain maps of the optical properties across the entire FOV of
92 *Bombus terrestris* compound eyes in unprecedented detail to explore the effect of body size on
93 the topological scaling of visual parameters.
94   Paradoxically, micro-CT generates more information than is currently feasible to
95 process, in particular, it provides a high level of detail about the geometry of the rhabdoms and
96 crystalline cones that has been left out of previous modelling approaches (e.g. Taylor et al.,
97 2019a, 2020). Information about the geometry of individual rhabdoms would enable optical
98 sensitivity calculations, and measuring the orientation of crystalline cones is crucial to produce
99 accurate estimates of the visual IO angle over the entire eye surface (Stavenga, 1979). This is
100 because crystalline cones are often skewed relative to the surface of the cornea, which is visible

101 in *Figure 1d* in Taylor et al. (2019a), so that the topology of their viewing directions determines
102 the angular spacing of neighbouring ommatidia (Baumgärtner, 1928; Stavenga, 1979). In other
103 words, measurements solely based on the angular spacing of facets on the eye surface, called
104 the corneal IO angle, generate biased estimates of resolution and FOV (Bergman and Rutowski,
105 2016; Taylor et al., 2019a). This difference is particularly striking at the edges of the FOV,
106 where corneal measurements of the IO angle often overestimate the actual visual IO angle
107 (Seidl and Kaiser, 1981; Taylor et al., 2019a). To address this problem, manual segmentation
108 (or labelling) of each crystalline cone 'by hand' in volumetric analysis programs is an option.
109 Unfortunately, unless it is possible to infer the elongation axes of the cones from their specific
110 geometry, as is the case in fiddler crabs (Bagheri et al., 2020), manual segmentation across
111 more than a few samples becomes nearly unfeasible for eyes that frequently consist of several
112 thousands of ommatidia. More generally, the current time-limiting factor of micro-CT is often
113 not the scanning itself but the volumetric analysis of the images it produces, particularly when
114 segmentation is required. If it is to become a widespread tool for large-scale anatomical studies
115 in arthropod vision, new methods are needed to automate the analysis of micro-CT scans.
116 　　　In this paper, we start to bridge this gap by developing a computing method,
117 *InSegtCone*, that segments crystalline cones in arthropod compound eyes with little input from
118 the user, i.e. nearly automatically. Our auto-segmentation method is based on an algorithm for
119 interactive segmentation (Dahl et al., 2020) that automatically labels repeated objects after a
120 short manual training. Here, we explore the functionality of *InSegtCone* by applying it to three
121 insect species with differently shaped apposition compound eyes: the Western honeybee *Apis*
122 *mellifera*, the buff-tailed bumblebee *Bombus terrestris*, and the green-veined white butterfly
123 *Pieris napi*. We demonstrate that the auto-segmentation process can successfully extract the
124 full shapes of 60%-80% of the total number of crystalline cones (~6000). We evaluate the
125 performance of the *InSegtCone* and compare it to manual labelling. We then discuss the
126 remaining limitations and new opportunities that this new technique generates.
127
128 **Material and Methods**
129
130 **Study animals**
131 Micro-CT image stacks of eye samples of adult workers (females) of *Apis mellifera* (specimen:
132 LU:3_14:AM_F_5) and *Bombus terrestris* (specimen: LU:4_16_: BT_F_CE_10) were the
133 same as those previously analysed in Taylor et al. (2019b), where the sample preparation and
134 data acquisition method are described in detail. An adult female of *Pieris napi* was obtained
135 from laboratory stock at the Department of Zoology, Stockholm University, Sweden.
136
137 **Sample preparation**
138 The left or right compound eyes of the bee specimens were dissected, fixated, stained, and
139 embedded in epoxy resin according to the procedure described in Taylor et al. (2019a). The
140 left half head of the sample of *P. napi* was fixated for 7 days at 4˚C in a 0.5% phosphotungstic
141 acid (PTA) solution (0.5 mg/mL of PTA in 70/30% ethanol/water solution) for staining. The
142 sample of *P. napi* was not embedded in resin but scanned directly in a 70% ethanol solution.
143
144 **X-ray microtomography (micro-CT)**
145 Micro-CT imaging of bee eyes was conducted at *Diamond Light Source* Beamline I13-2 (Peić
146 et al., 2013; Rau et al., 2011), Harwell Science and Innovation Campus, Oxfordshire (UK).
147 The voxel size of the bee eyes was 1.6 µm. A detailed description of the scanning procedure
148 can be found in Taylor et al. (2019a).
149 　　　The *P. napi* sample was scanned at the *Stockholm Brain Imaging Center - SUBIC*
150 (Lacerda and Lindblom, 2014) at Stockholm University (Sweden) using the 3D submicron

151 imaging system Xradia Versa 520 (Zeiss, Jena, Germany). The imaging was performed with
152 the X-ray source running with a voltage of 80 kV and a power of 7 W. A 4x optical objective
153 was used, combined with the geometrical magnification, leading to an effective voxel size of
154 1.08 µm. The tomography contained 2401 projections over 360˚. The exposure time was 1 s
155 per projection. The projection images were then reconstructed automatically using the Zeiss
156 Scout-and-Scan software.
157
158 **Volumetric segmentation of the eye and the external cornea**
159 To perform the auto-segmentation of the cones, *InSegtCone* required input labels of key eye
160 features that were extracted from the reconstructed microCT images. The external cornea and
161 the full eye volume of each compound eye were labelled by volumetric segmentation in Amira
162 (FEI, Hillsboro, USA) using a method modified from Taylor et al. (2019a) . The original 32-
163 bit images reconstructed from the scans were cropped and re-saved in 8-bit files in the program
164 Drishti Paint (Limaye, 2012). The images were resampled to 4 µm voxels. The eye volume
165 was labelled thanks to a combination of automatic thresholding, filling of holes on each slice,
166 shrinking and growing of the labelled volume, and selection of connected components. The
167 outer surface of the cornea was extracted from the eye label by manually drawing a geodesic
168 path at the border of the cornea and extracting the enclosed surface. The two labels were saved
169 as volumetric images for later analysis in MATLAB (The MathWorks Inc., USA).
170
171 **Manual segmentation of the crystalline cones**
172 Crystalline cones were labelled manually in the full-resolution 8-bit images using the brush
173 tool of Amira across 2D slices. Care was taken to obtain a collection of segmented cones
174 distributed as uniformly as possible across the eye. To compare with the segmentation time of
175 the automatic method, the time required for a user to perform manual segmentation of the cones
176 of *P. napi* in Amira was estimated.
177
178 **Automatic segmentation of the crystalline cones**
179 The schematic of the automatic segmentation (or auto-segmentation) process of the crystalline
180 cones called *InSegtCone* is described in *Figure 1*. The process was performed in MATLAB
181 and the code is available for download on *Github* (link will be provided before publishing).
182 The main innovative aspect of the segmentation method consists in the unfolding of the original
183 eye volume into a 2D coordinate system referenced to the external surface of the cornea. This
184 simplifies the segmentation problem, as the actual texture-based segmentation (Dahl et al.,
185 2020) can then take place in two instead of three dimensions. To allow accurate unfolding,
186 despite the variable curvature of the external surface of the cornea, the eye was divided into
187 sub-regions prior to the unfolding. The effect of this step on the performance of the method
188 was tested by independently applying the auto-segmentation method to the eye of *A. mellifera*
189 divided into increasing numbers of sub-regions (1, 2, 4, 6, 9, 12). The eye of *B. terrestris* (resp.
190 *P.napi*) was divided into 12 (resp. 9) sub-regions.
191   The crystalline cone auto-segmentation process consisted of six steps: *(a)* reorientation
192 of the eye; *(b)* division of the outer cornea voxels into sub-regions and surface modelling using
193 polynomial fitting; *(c)* extraction and unfolding of a sub-volume of the data capturing the
194 crystalline cone layer; *(d)* auto-segmentation of the cones using a texture-based approach; *(e)*
195 back-transformation of the segmented labels into the original space; *(f)* post-processing to
196 identify the valid cones. The details of each step are described below. The mathematical
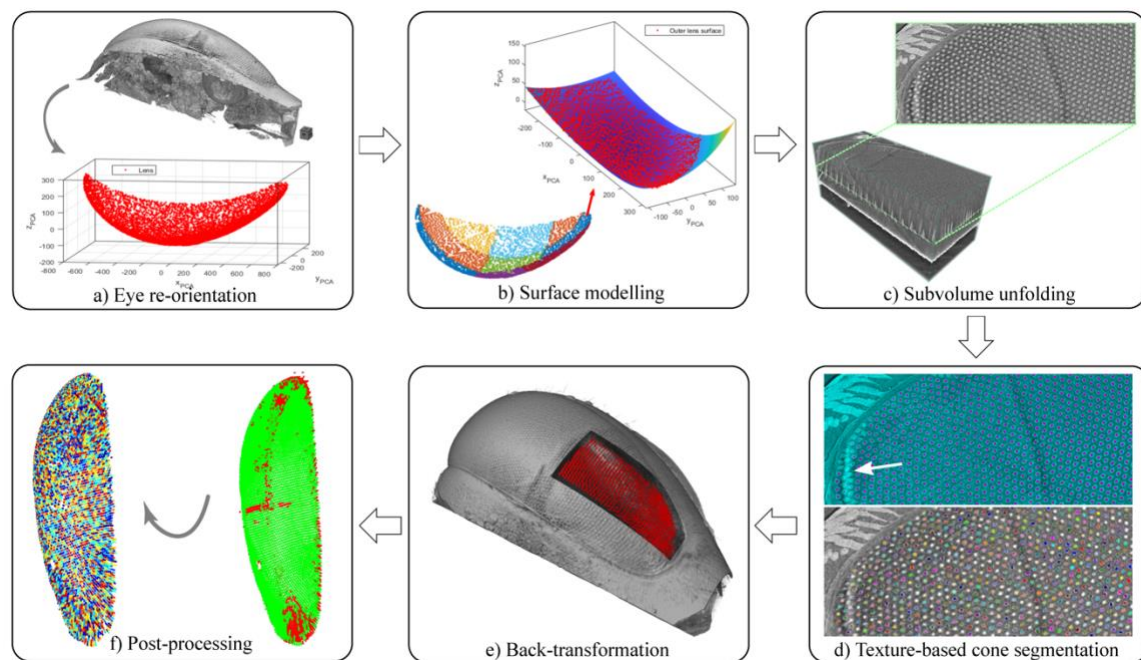197 explanation of each step is given in supplementary.
198

4

199
200 *Figure 1:* Outline of the process to automatically segment crystalline cones. The method is illustrated with images
201 of *Apis mellifera* as an example. *(a)* Reorientation of the eye (volume rendering) and the labelled external cornea
202 (red) into the 'PCA space'. *(b)* Division of the cornea surface voxels into subregions (each plotted with a different
203 colour) and modelling of each subregion using polynomial fitting in its 'PCA space' (top). *(c)* Extraction and
204 unfolding of a subvolume of the eye data. Note that the cornea surface in the unfolded subvolume is almost flat,
205 so that the pattern of crystalline cones in the cross-section is regular. *(d)* Auto-segmentation of the raw cones
206 using a texture-based approach. The results of this step are displayed on one slice from the unfolded images (top)
207 and in the whole eye subvolume (bottom). The white arrow indicates the location of a circular artefact that locally
208 prevented the segmentation of a few cones. *(e)* Back-transformation of the raw auto-segmented cones into the
209 original eye volume (3D rendering). *(f)* Post-processing of the raw cones labels (right subfigure) to eliminate noisy
210 detections (red on the right subfigure) and retain valid cones (green on the right subfigure - left subfigure).

211
212 *(a)*   *Global alignment of the eye*
213 In general, the position and orientation of the eye in the volumetric data is arbitrary, depending
214 on how the sample was mounted during scanning. However, later steps of the analysis rely on
215 the eye surface being approximately aligned with the *xy*-plane. Therefore, the first step of the
216 analysis is to rotate the eye.
217   To align the eye, we used the previously segmented (see *Volumetric segmentation of*
218 *the eye*) volumetric images (*tiffs*, *nifty*, or any other image file format), where voxels labeled
219 as cornea formed a point cloud that represented the surface of the eye. Using Principal
220 Component Analysis (PCA), as shown in *Figure 1a,* the eye was rotated to have the longest
221 side (first principal component) aligned with the *x*-axis, and the external-to-internal (or
222 proximodistal) direction (third principal component) aligned with the *z*-axis. This step allows
223 for a more systematic procedure that facilitates comparison and automation by transforming
224 the set of points corresponding to the label of the external surface of the cornea into a coordinate
225 system called 'PCA space', (x', y', z').

226
227 *(b)*   *Division into sub-regions, local alignment and surface modelling*
228 The goal of this step is to obtain a sensible 2D coordinate system of the compound eye by
229 building a 3D polynomial surface model for the external cornea voxels. For the eyes that have
230 high curvature, such as the *Pieris napi* sample that has an almost hemispherical eye, it would
231 be difficult to achieve an accurate polynomial fitting on the complete external cornea. We

5

232 therefore divided the external surface of the cornea of such highly curved eyes into sub-regions
233 in the 'PCA space'. Practically, the division of the external surface of the cornea can be realized
234 by defining a grid of 2D rectangular masks in the dimension of (x', y'), with a small overlapping
235 area at the borders of the sub-regions, in order to avoid the loss of cones near the borders of
236 the sub-regions in later steps.
237   The cornea surface in each sub-region was then locally aligned by preforming a PCA-based
238 rotation as in *(a)*. With the eye surface roughly aligned with the *xy*-plane, we could fit a
239 polynomial surface $z=f(x,y)$ to the voxels labelled as cornea. We chose to fit a fifth order
240 polynomial surface. An example of the surface fitting on a sub-region of the honeybee eye is
241 displayed in *Figure 1b*.

243 *(c)   Sub-volume extraction and unfolding*
244 The purpose of this process is to extract a sub-volume of the original data volume including
245 the crystalline cone layer in each sub-region.
246   As the external sub-surface of the cornea is now modelled as a polynomial function, it
247 could be resampled to a matrix of points with a density that offers sufficient resolution and
248 optimizes the computational time. Each sub-surface sample point was then paired with a unit
249 direction vector that was defined as the surface normal at the sample point on the cornea and
250 pointing towards the inside of the eye. By sampling along the unit vectors, we obtain a sub-
251 volume aligned with the "flattened" cornea surface within a defined displacement along the
252 cornea surface normal.
253   In order to extract the intensity of the query points, they are back-transformed to the
254 original coordinate system, and the image intensity is sampled from the data volume, using
255 tricubic interpolation. Due to the step-wise extraction of displaced cornea layers, the sub-
256 volume is in some sense "unfolded", as illustrated in *Figure 1c*.

258 *(d)   Texture based auto-segmentation of the cones*
259 In the unfolded sub-volumes, the crystalline cones should ideally appear as 'cylinders' aligned
260 with the z-axis (the displacement layers), with a predictable repeated pattern of small circular
261 structures. The segmentation of cones is thus simplified to a two-dimensional problem.
262   In this paper, we chose the texture-based segmentation tool *InSegt* (Dahl et al., 2020).
263 To train *InSegt*, a user selected a single slice from the unfolded volume. This slice should be
264 within the crystalline cone layer. The user provided a sparse manual annotation of this slice by
265 marking some pixels as belonging to the background class, and some pixels as belonging to
266 the cone class. The corresponding full segmentation of the slice is presented to the user for
267 inspection, such that labelling continues until segmentation is satisfactory (cyan and magenta
268 overlay in *Figure 1d, movie S1*). Based on this input, a dictionary was trained and applied to
269 all other slices in the unfolded sub-volume.

271 *(e)   Back-transformation*
272 The labelled voxel coordinates were finally mapped back into the original coordinate system,
273 using the transformation described in supplementary Equation 1. A label containing multiple
274 raw segmented cones in the original 3D image was thus obtained (*Figure 1e*).

276 *(f)   Post-processing of the raw cones*
277 The automatically segmented labels unavoidably contain pixels that are not cones. A post-
278 processing is necessary to exclude noisy detections while keeping as many correctly segmented
279 cones as possible *(Figure 1f)*. In order to differentiate, the automatically segmented labels
280 before post-processing are hereby called "raw cones". The post-processing was divided into

6

281 three main steps: identification of the individual raw cones, calculation of the raw cone
282 characteristics, stepwise elimination of noisy detections *(Figure S1)*.

283   i. Identification of individual raw cones
284   A connected component analysis in the original coordinate system was performed to
285   detect and individually label each raw cone (some of which are artefacts).

286   ii. Calculation of raw cone characteristics
287   A PCA was performed on each raw cone to calculate its geometric properties and detect
288   outliers. The coefficients, eigenvalues of the covariance matrix and estimated mean
289   were used to calculate its *elongation axis*, *length* and *radius*, and *cone centre*,
290   respectively. The sign of the *elongation axis* was chosen so that it points towards the
291   surface of the cornea. The *cone size* was the number of voxels included in the raw cone
292   volume. The *distance to neighbouring cones* was the average distance between the raw
293   cone centre and the centres of the three closest neighbouring raw cones.

294   iii. Stepwise elimination of noisy detections
295   In this part, the cone characteristics were used to detect outliers in four consecutive
296   sorting steps:

297   1. Raw cones with a *cone size* lower than ten voxels were immediately removed
298   because they were likely to be noisy detections.

299   *2.* As in an earlier step (see *Modelling of the outer cornea surface*), the coordinates of
300   the *cone centres* were transformed in the 'PCA space' given by the coefficients of
301   a PCA of the cornea surface in each eye sub-region. A polynomial fitting (method
302   *poly55*) was implemented on the normalised transformed *cone centres* using the *z*-
303   component as a dependent variable. In each eye sub-region, the residuals of the
304   polynomial fitting were used to cluster the cone candidates into one, two or three
305   groups according to the gaussian mixture model (function *fitgmdist*) with the best
306   Akaike Information Criterion (AIC). The user then indicated through visual
307   inspection which groups of raw cones appeared valid in each eye subregion. Invalid
308   cones generally stick out from the clusters of valid cones that gradually follow the
309   eye curvature, making visual inspection relatively fast (~2 min per specimen) and
310   straightforward. Groups of raw cones that were not validated by the user were
311   discarded in the following steps.

312   *3.* The coordinates of the remaining *cone centres* were transformed into the coordinate
313   system now given by the coefficients of a PCA of the full cornea surface. Five
314   polynomial (*poly55*) fittings were implemented in the *(x, y)* components of the *cone*
315   *centres* on the following dependent variables: normalised *z*-component of the *cone*
316   *centres, size*, *length*, *radius* and *distance to neighbouring cones*. These variables
317   were chosen for the detection of outliers because they are conserved in the true
318   cones (expect from small topological variations) but stand out in the noisy
319   detections. The detailed procedure for the detection of outlier is provided in *Text*
320   *S1*.

321   *4.* A final polynomial fitting (*poly55*) was implemented on the *cone centres* of the
322   remaining raw cones. A linkage was computed to determine the proximity of the
323   fitted *cone centres* onto the polynomial surface. This linkage was used to define
324   clusters of fitted *cone centres* that were closer than the *cut-off distance*. The *cut-off*
325   *distance* was set by the user at 13 µm for all specimens because the average distance
326   between ommatidia is approximately 20 µm in these specimens, such that two cones
327   separated by less than a *cut-off distance* are abnormally close. In each cluster of
328   fitted *cone centres*, the raw cone that had the largest fitting residual was eliminated
329   iteratively until the distance between all the fitted *cone centres* in the cluster was
330   greater than the *cut-off distance*.

331   The raw cones that had not been disqualified throughout the four elimination steps were
332   classified as valid cones.
333

Performance of the auto-segmentation process

335 To assess the performance of *InSegtCone*, five metrics were calculated. The surface modelling
336 error and angular discrepancy between automatic and manual segmentation reflect the accuracy
337 of the method (using manual segmentation as a reference), whereas the segmentation time,
338 percentage of auto-segmented cones and local cone density ratio of cones reflect the efficiency
339 of the method.

340 *(a) Surface modelling error*
341   During surface modelling (see *division into subregions and surface fitting*), the *surface
342   modelling error* was calculated as the average of the root mean squared error (rmse) of the
343   polynomial fittings of the surface of the cornea across each of the eye sub-regions.

344 *(b) Segmentation time of the auto-segmentation method*
345   To evaluate the performance of the auto-segmentation method, the segmentation time of
346   the process was estimated. The volumetric segmentation of the eye is probably the most
347   time-consuming step of the analysis (2-4 hours per specimen), but was not taken into
348   account here because it is a prerequisite but not a part of the auto-segmentation of the cones.
349   The segmentation time of the auto-segmentation process was thus approximately equal to
350   the longest step – the texture-based auto-segmentation. When evaluating the texture-based
351   segmentation duration, we considered only the cumulated time spent by the user to
352   manually annotate and train the segmentation model on each eye sub-region. The rest of
353   the computing time for automatic segmentation using the trained dictionary highly depends
354   on the size of the image data and the computer power, therefore it is not discussed in detail
355   here.

356 *(c) Percentage of auto-segmented cones*
357   This was the number of valid cones after post-processing divided by the predicted number
358   of ommatidia that was obtained using the method described in Taylor et al. (2019a). In
359   brief, manual measurements of facet diameters at about 30 locations across the eye were
360   used to build an interpolant of facet area across the eye surface. The predicted number of
361   ommatidia is thus the total area of the cornea surface estimated from an *isosurface fit*
362   (function *isosurface* with *isovalue = 0.5*) divided by the average interpolated facet area.

363 *(d) Angular discrepancy between automatic and manual segmentation*
364   The same cone can be segmented both manually in Amira and with the auto-segmentation
365   method, thus generating two *cone duplicates*. This was considered to be the case if the *cone
366   centre* of an auto-segmented cone was less than a voxel away from a manually segmented
367   cone. The angular discrepancy between automatic and manual segmentation was the angle
368    $\alpha \in [0, \pi]$, between the elongation axes of the two *cone duplicates*.

369 *(e) Local cone density ratio*
370   The local cone density ratio $R \in [0, 1]$, represents the local coverage of the auto-
371   segmentation method. A ratio equal to 1 indicates that all cones predicted locally were
372   identified and segmented by the method. To calculate R, equidistant sampling points on the
373   cornea surface were obtained as in Taylor et al. (2019a) . The local density ratio at each
374   sampling point was the number of cones identified by the auto-segmentation method within
375   a given range (100 µm) divided by the expected number of ommatidia in the same range.
376   The latter was the local area of the cornea subset divided by the local average facet area.
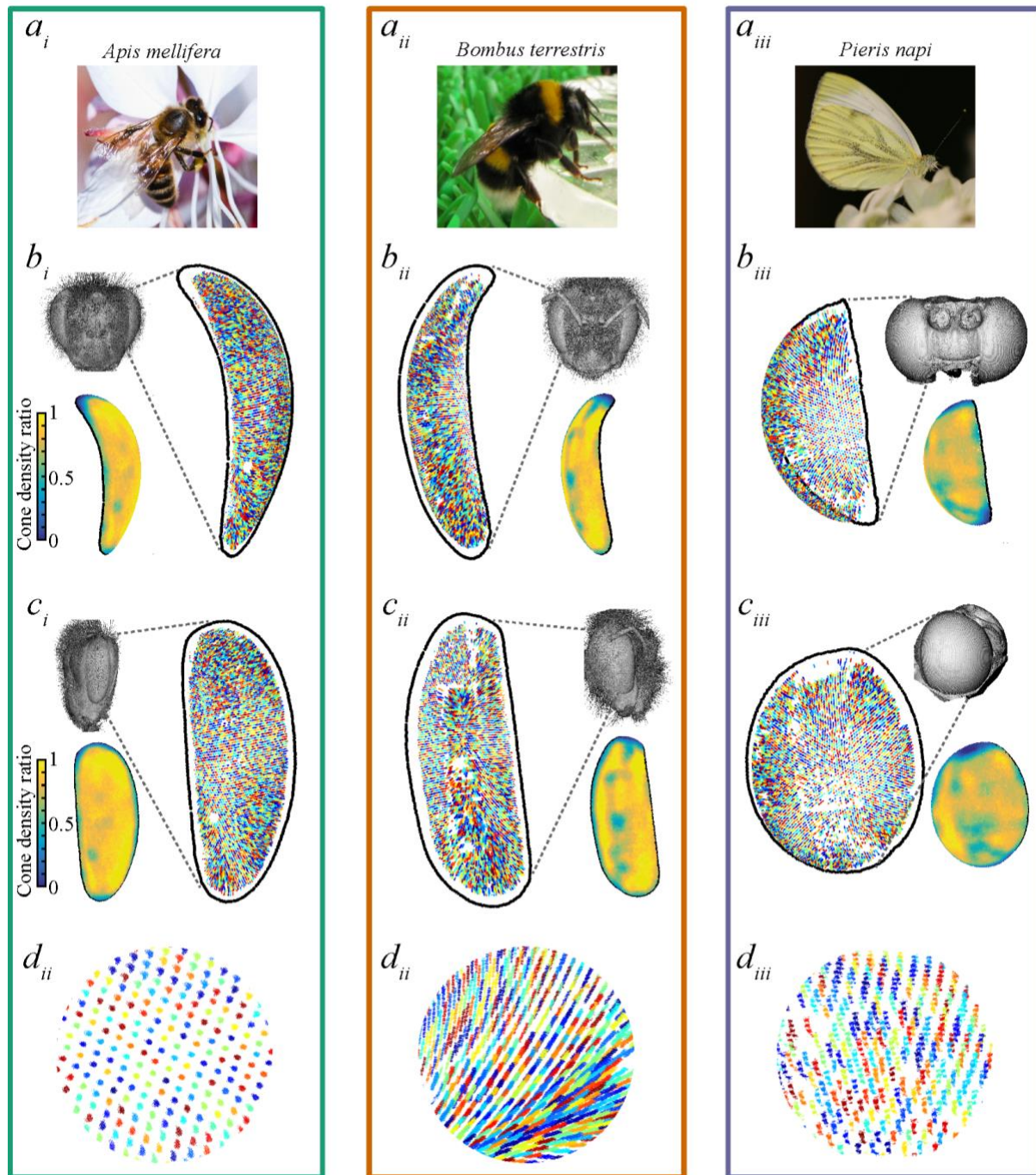377

378

Results

380

Figure 2: Auto-segmented crystalline cones in the compound eyes of three arthropods. The eyes of *Apis mellifera* (a_i), *Bombus terrestris* (a_{ii}) and *Pieris napi* (a_{iii}) were divided respectively into 4, 12 and 9 subregions. Overview of the cones segmented with *InSegtCone* (each labelled with a different colour) from the front *(b_{i-iii})* and the side *(c_{i-iii})*, as indicated by the volume renderings of the species' heads (grey images). The border of the external surface of the cornea is represented in black. The miniature in each left corner indicates the topology of the cone density ratio. A ratio locally equal to one means that all expected cones were auto-segmented. *(d_{i-iii})* Detailed view of a portion of the auto-segmented cones.

When applied to compound eyes of *Apis mellifera*, *Bombus terrestris* and *Pieris napi*, *InSegtCone* enabled the automatic reconstruction of 4423, 3783 and 4334 cones, corresponding to 80%, 76% and 62% of the predicted total number of crystalline cones, respectively (*figure*

9

393   *2* and *figure 3c, movies S2-4*). The cone density ratio *R*, i.e. the local ratio of auto-segmented
394   over predicted cones, was close to 1 across most regions of the eyes of *A. mellifera* and *B.*
395   *terrestris*, indicating that all the cones predicted in these areas were segmented (*figure 2*). The
396   value of *R* dropped in the most dorsal region and at the edges of the eye, indicating that the
397   cones that remained undetected were situated in these areas (representing ~20% of the total
398   number of cones). The topography of *R* was more irregular in *Pieris napi*, revealing small areas
399   where cones were not segmented, in the most dorsal and ventral regions and at the edges of the
400   compound eye.
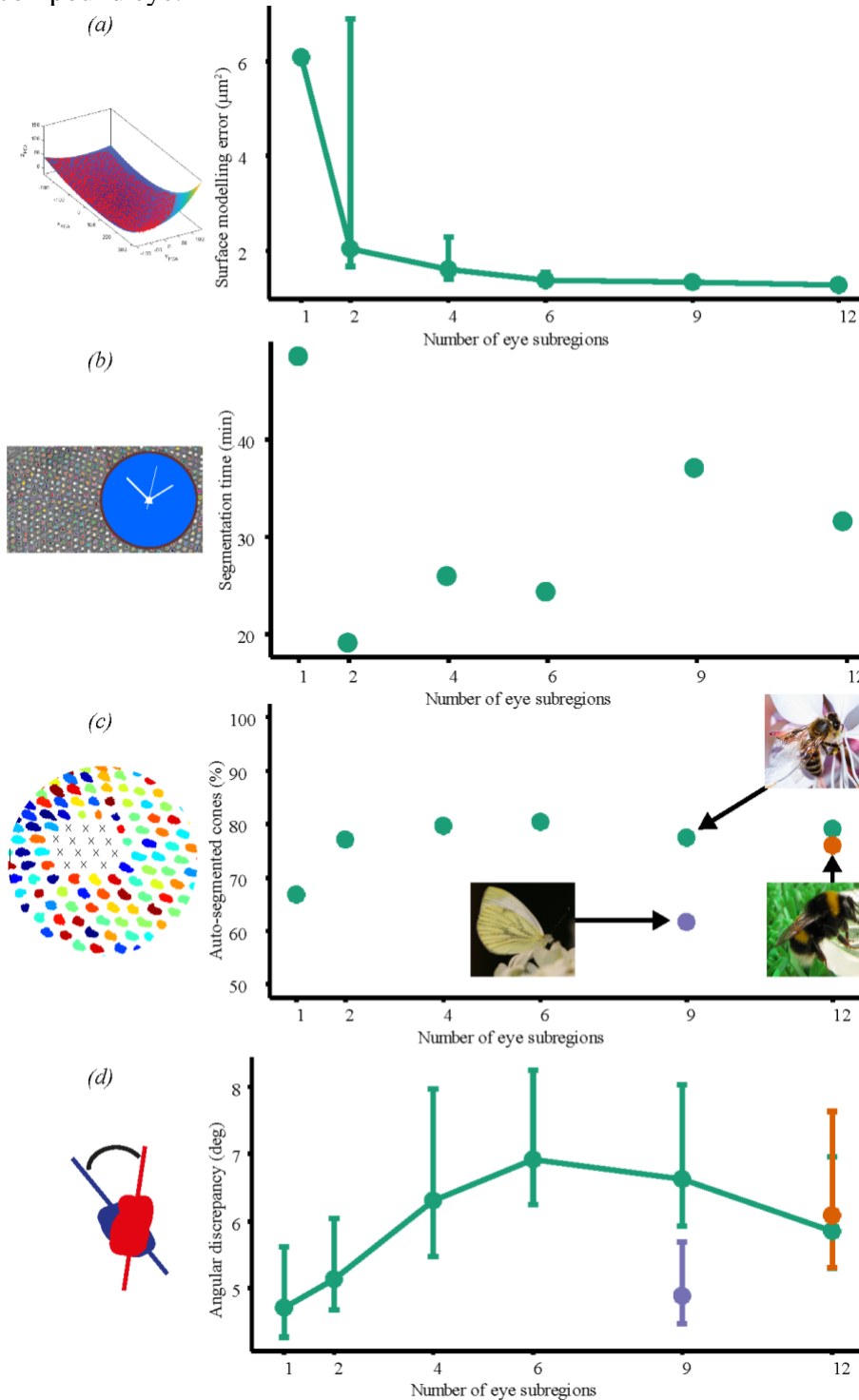
401
402   *Figure 3:* Performance of the auto-segmentation method in *Apis mellifera* (green), *Bombus terrestris* (orange) and
403   *Pieris napi* (purple). The surface modelling error *(a)*, segmentation time *(b)*, percentage of auto-segmented cones
404   *(c)* and angular discrepancy between manual and auto-segmentation *(d)*, are represented as a function of the

10

405 number of eye subregions used in the segmentation algorithm. When drawn, error bars represent the standard
406 error around the mean values.

407

408 Once the segmentation of the eye and cornea (that requires most manual work) were
409 completed, the segmentation time of the automatic method was ~30 min for ~4400 cones
410 (*figure 3b*), whereas the duration of the manual segmentation was ~180 min for 100 cones
411 (table S1). This means that the manual method permitted the segmentation of one cone in about
412 2 min when the automatic method segmented one cone in less than 0.5 s.
413 To test the effects of dividing the eye into sub-regions, the auto-segmentation process
414 was applied to the compound eye of *A. mellifera* when it had been divided into increasing
415 numbers of sub-regions N_{SR}. The aim of this test was also to identify the optimal N_{SR} that trades
416 off accuracy and efficiency. The percentage of segmented cones initially increased with
417 increasing N_{SR} ($N_{SR} \in [1, 4]$, *figure 3c*), until it reached a plateau and even slightly dropped
418 ($N_{SR} \in [4, 12]$, *figure 3c*). This initial gain highlights the benefits of dividing the eye into sub-
419 regions, and was due to the segmentation of additional cones in the dorsal area of the compound
420 eye (*figure S2*). This was likely facilitated by the initial decrease of the surface modelling error
421 (*figure 3a*). The improved efficiency of the algorithm up to $N_{SR} = 4$ did not increase the run-
422 time of the auto-segmentation process (*figure 3b*), although it may have caused a slight increase
423 in the average angular discrepancy between the automatic and the manual segmentation (*figure
424 3d*).
425 The angular discrepancy α between automatic and manual segmentation, that is the
426 angle between the elongation axes of the manually and the auto-segmented duplicates of the
427 same cone, could locally be close to 70 deg (*figure S4*). Note that this does not indicate that the
428 auto-segmented cone is 70 deg off the elongation axis, as manual segmentation is also prone
429 to errors. Moreover, α was on average below 7 deg for all eyes (*figure 3d*), which indicates a
430 good agreement between the manual and the auto-segmentation methods overall.

431
432

Conclusion

434
435

436 In this paper, we demonstrate *InSegtCone,* a new computational method for automatically
437 segmenting the crystalline cones of compound eyes in arthropods using high-resolution micro-
438 CT images. We assessed the performance of the method by implementing the auto-
439 segmentation process on the apposition compound eyes of three insect species. Our method
440 labelled most of the crystalline cones across of the compound eyes and generated cone labels
441 with a similar level of accuracy than manual segmentation but ~250 times faster. We conclude
442 that this new method for auto-segmentation of crystalline cones is accurate and efficient.
443 *InSegtCone* sets the ground for subsequent high-throughput analyses that are required for
444 understanding the diversity of eyes and vision in arthropods.

445

Current limitations and possibilities for improvement

447

448 Because the present automatic procedure is ~250 times faster than manual labelling, it greatly
449 facilitates the segmentation of crystalline cones and minimises most of the labour-intensive
450 manipulations usually required for such analyses. However, the method still requires some
451 level of manual interaction with the user, in particular, during the segmentation of the external
452 surface of the cornea and the texture-based segmentation that requires the annotation of
453 crystalline cones on a 2D slice (if no existing dictionary from similar samples is available).

11

454 There are thus opportunities for further automation of the segmentation process. We encourage
455 future users to carefully consider the advantages of using the auto-segmentation instead of a
456 manual segmentation method. The automatic method is probably most beneficial when applied
457 to numerous eye samples and/or species with many ommatidia (and thus many cones), such as
458 the bees and butterfly presented in this paper that possess several thousands of ommatidia.
459 Manual segmentation may be more advantageous for studies restricted to few specimens of
460 arthropods with a small number (<100) of ommatidia (Taylor et al., 2020).
461 Our auto-segmentation tool uses clustering of image features and manual labelling from
462 one slice to segment repeated patterns (here, in the form of small circles). It will perform well
463 on images that have a similar appearance as the image used for training the dictionary.
464 However, micro-CT reconstructions sometimes generate artefacts (e.g. ring artefacts, beam
465 hardening, etc.) that affect the appearance of the cones and can locally disrupt the auto-
466 segmenting of cones. An example of this is indicated by the arrow in *figure 1d* where the
467 algorithm failed to segment the cones around the stripes caused by ring artefacts. Fortunately,
468 micro-CT is a non-destructive imaging method that allows repeated scanning on the same
469 specimen with adjusted parameters to enhance image quality and limit artefacts. The image
470 quality can also be improved during reconstruction with numerous post-processing tools, such
471 as ring removal algorithms (Vo et al., 2018).
472 During the texture-based segmentation step, a *training dictionary* is built from the
473 manual annotation of a training slice (Dahl et al., 2020). If the cross sections of the cones have
474 a highly variable appearance across the slice, the use of a unique training dictionary common
475 to all the cones is likely to lead to inaccurate or poor segmentation results. The variable
476 appearance of cones across a training slice can have several explanations. For example, *(1)* if
477 the thickness of the cornea significantly changes across the eye, the training slice will contain
478 cones that appear different because they are viewed at different positions along their main
479 elongation axes. This issue may be avoided by using a more robust reference for surface
480 modelling, such as the internal, instead of the external, corneal surface, although this would
481 require additional volumetric segmentation efforts. Another solution is to divide the compound
482 eye into a higher number of sub-regions to ensure that the thickness of the cornea is
483 homogeneous within each sub-region. *(2)* The cones themselves can have distinct
484 morphologies in different regions. For instance, the cones located in the dorsal area of the bee
485 eyes appear to be shorter and more densely packed than in the rest of the eye (*figure 2*). In this
486 case, a sub-region dedicated to these challenging regions may be needed to improve
487 segmentation. *(3)* Auto-segmentation can be complicated if neighbouring crystalline cones are
488 in contact with each other, such as in the case of crab compound eyes (Alkaladi and Zeil, 2014;
489 Bagheri et al., 2020). In this case, the texture-based segmentation algorithm either fails, or the
490 cones are segmented together in a bundle of connected voxels and cannot be isolated without
491 additional post-processing, e.g. morphological erosion and dilation techniques (Gonzalez et al.,
492 2004). An alternative solution is to combine the texture-based segmentation with shape
493 recognition algorithms, such as circle detection (Gonzalez et al., 2004).
494
495 **Current and future Applications**
496
497 Despite the limitations discussed above, *InSegtCone* represents a formidable opportunity for
498 the study of the visual biology of arthropods. Because it greatly accelerates time-consuming
499 labelling, this new tool enables comprehensive studies across a large number of arthropod eyes,
500 which had been practically inaccessible until now. The auto-segmentation method also has a
501 wide range of potential applications within and beyond the study of the anatomy of compound
502 eyes. Firstly, (and possibly most obviously) the labels of the crystalline cones can serve to
503 generate unbiased functional optical models of the eyes. This is because, without analysis of

the crystalline cones, optical models must be based on the apparent angular spacing of facets on the external surface of the cornea, the corneal IO angle, which produces biased estimates of optical resolution and of the field of view (FOV) of the eye (Bergman and Rutowski, 2016; Taylor et al., 2019a). The auto-segmented labels can be used to estimate the skew β between the normals to the external cornea and the main *elongation axes* of the crystalline cones across the compound eye (Stavenga, 1979). The cone skew β is then necessary to compute the visual IO angle – an unbiased estimate of optical resolution– that can be mapped across the accurately delineated FOV of the eye. Ultimately, the fast auto-segmentation method makes it possible to compare theses accurate resolution maps across large numbers of specimens with different sizes, life-stages, sex, species, etc. This is likely to advance our understanding about the visual ecology and evolution of vision in arthropods (Bagheri et al., 2020; Scales and Butler, 2016; Somanathan et al., 2009; Taylor et al., 2019a). The auto-segmentation method not only extracts the *elongation axis* of the crystalline cones but also their full shape. This is interesting because several arthropod species modify the length (Brodrick et al., 2020; Menzi, 1987; Nilsson and Odselius, 1981) and the diameter (Brodrick et al., 2020) of their crystalline cones in response to changes in light levels. In fiddler crabs, these light-adaptation mechanisms together with modifications of the rhabdoms enhance optical sensitivity at night (Brodrick et al., 2020). The auto-segmentation method generates opportunities for large scale investigation of these light-adaptation properties at numerous light levels and across large numbers of species.

Applying the auto-segmentation method to other parts of the eyes could facilitate the labelling of other elements in the compound eyes. For instance, the centre of individual facets could be identified automatically by running the program superficially over the external surface of the cornea. This technique would promptly generate 3D maps of facet dimensions across the eye and thus good estimates of the total number of ommatidia. The program could be adapted to extract morphological properties of the rhabdoms when they are visible, i.e. when the resolution and contrast of micro-CT images are sufficient. This would represent a great benefit given that current studies of rhabdom morphology require tedious sample preparation and slicing for Transmission Electron Microscopy. A modified version of the auto-segmentation method could be used to measure the diameter of rhabdom, either by using the proximal tip of the segmented crystalline cone, or directly by segmenting the rhabdom shape. Besides being more accurate, the latter method would have the additional advantage of extracting other properties, such as the length of the rhabdoms. To segment rhabdoms, we expect better results using the retina-cone interface as a reference during the surface modelling step, rather than the external surface of the cornea. With these measurements of rhabdom diameters and lengths, scientists would be able to calculate the topology of optical sensitivity with unprecedent level of detail across the eye.

Finally, *InSegtCone* could solve segmentation problems beyond the study of compound eyes. In micro-CT scans of camera-type eyes, such as ocelli (Wilby et al., 2019), this represents a promising tool for fast reconstruction of the shape of photoreceptors across the retina. In principle, our method can be extended to label photoreceptors on any tomographic reconstruction of vertebrate or invertebrate retina, regardless of the imaging technique involved to generate data (micro-CT, confocal microscopy, etc). More generally, this work can inspire projects in a wide range of fields that require tools to segment repeated elements in a 3D layer. In Biology, these repeated elements are for example: muscle fibres, olfactory sensilla on antennas, epidermal appendages such as scales, vascular tissue and roots of plants. The first part of the process involving the modelling of the external cornea may also inspire other studies to achieve better visualization or easier quantitative analysis through the unfolding of 3D images.

13

Acknowledgments

Competing interests

The authors declare that they have no competing interests.

Data availability

The original image data of the compound eyes as well as the manual and automatic cone labels will be made available on *MorphoSource* prior to publication. The raw data used to evaluate the performance of the method will be available on *Dryad*. The MATLAB scripts used for the auto-segmentation process will be made available on *Github* upon publication.

Author contributions

All authors designed the study. HMK, TZ and PT collected the data and generated the analyses. HMK, TZ and PT drafted the manuscript. All authors revised the manuscript.

References

Alkaladi A, Zeil J. 2014. Functional anatomy of the fiddler crab compound eye (Uca vomeris: Ocypodidae, Brachyura, Decapoda). *J Comp Neurol* **522**:1264–1283. doi:10.1002/cne.23472

Bagheri ZM, Jessop A-L, Kato S, Partridge JC, Shaw J, Ogawa Y, Hemmi JM. 2020. A new method for mapping spatial resolution in compound eyes suggests two visual streaks in fiddler crabs. *J Exp Biol* **223**:jeb210195. doi:10.1242/jeb.210195

Baird E, Taylor G. 2017. X-ray micro computed-tomography. *Curr Biol* **27**:R289–R291. doi:10.1016/j.cub.2017.01.066

Baumgärtner H. 1928. Der Formensinn und die Sehschärfe der Bienen. *Z Vgl Physiol* **7**:56–143. doi:10.1007/BF00341153

Bergman M, Rutowski RL. 2016. Eye morphology and visual acuity in the pipevine

602   swallowtail (Battus philenor) studied with a new method of measuring interommatidial
603   angles. *Biol J Linn Soc* **117**:646–654. doi:10.1111/bij.12694
604 Berry RP, Stange G, Warrant EJ. 2007. Form vision in the insect dorsal ocelli: An anatomical
605   and optical analysis of the dragonfly median ocellus. *Vision Res* **47**:1394–1409.
606   doi:10.1016/j.visres.2007.01.019
607 Brodrick EA, Roberts NW, Sumner-Rooney L, Schlepütz CM, How MJ. 2020. Light
608   adaptation mechanisms in the eye of the fiddler crab Afruca tangeri. *J Comp Neurol*
609   cne.24973. doi:10.1002/cne.24973
610 Cronin TW, Johnsen S, Marshall J, Warrant EJ. 2014. Visual Ecology. Princeton and Oxford:
611   Princeton University Press.
612 Dahl VA, Trinderup CH, Emerson MJ, Dahl AB. 2020. Content-based Propagation of User
613   Markings for Interactive Segmentation of Patterned Images.
614 Gonzalez RC, Woods RE, Eddins SL. 2004. Digital image processing using MATLAB.
615   Pearson Education India.
616 Lacerda F, Lindblom B. 2014. SUBIC : Stockholm University Brain Imaging
617   CenterFONETIK 2014. Stockholm: Department of Linguistics.
618 Land MF. 1997. visual acuity in insects. *Annu Rev Entomol* **42**:147–177.
619   doi:10.1146/annurev.ento.42.1.147
620 Land MF, Nilsson D-E. 2012. Animal Eyes, Oxford Animal Biology Series. Oxford
621   University Press. doi:10.1093/acprof:oso/9780199581139.001.0001
622 Limaye A. 2012. Drishti: a volume exploration and presentation tool. *Dev X-Ray Tomogr*
623   *VIII* **8506**:85060X. doi:10.1117/12.935640
624 Menzi U. 1987. Visual adaptation in nocturnal and diurnal ants. *J Comp Physiol A*.
625 Nilsson D, Odselius R. 1981. of Comparative A New Mechanism for Light-Dark Adaptation
626   in the Artemia Compound Eye (Anostraca , Crustacea) *. *J Comp Physiol*.
627 Peić ZD, De Fanis A, Wagner U, Rau C. 2013. Experimental stations at I13 beamline at
628   Diamond Light SourceJournal of Physics: Conference Series. IOP Publishing. p.
629   182003. doi:10.1088/1742-6596/425/18/182003
630 Rau C, Wagner U, Pešić Z, De Fanis A. 2011. Coherent imaging at the Diamond beamline
631   I13. *Phys Status Solidi Appl Mater Sci* **208**:2522–2525. doi:10.1002/pssa.201184272
632 Roskov Y, Abucay L, Orrell T, Nicolson D, Kunze T, Culham A, Bailly N, Kirk P, Bourgoin
633   T, DeWalt RE, others. 2000. Species 2000 & ITIS catalogue of life, , 2020-08-01 Beta.
634 Scales JA, Butler MA. 2016. The relationship between microhabitat use, allometry and
635   functional variation in the eyes of Hawaiian Megalagrion damselflies. *Funct Ecol*
636   **30**:356–368. doi:10.1111/1365-2435.12479
637 Seidl R, Kaiser W. 1981. Visual field size, binocular domain and the ommatidial array of the
638   compound eyes in worker honey bees. *J Comp Physiol ? A* **143**:17–26.
639   doi:10.1007/BF00606065
640 Somanathan H, Borges RM, Warrant EJ, Kelber A. 2017. Visual Adaptations for Mate
641   Detection in the Male Carpenter Bee Xylocopa tenuiscapa. *PLoS One* **12**:e0168452.
642   doi:10.1371/journal.pone.0168452
643 Somanathan H, Kelber A, Borges RM, Wallén R, Warrant EJ. 2009. Visual ecology of Indian
644   carpenter bees II: adaptations of eyes and ocelli to nocturnal and diurnal lifestyles. *J*
645   *Comp Physiol A* **195**:571–583. doi:10.1007/s00359-009-0432-9
646 Stavenga DG. 1979. Pseudopupils of Compound Eyes. pp. 357–439. doi:10.1007/978-3-642-
647   66999-6_7
648 Taylor GJ, Hall SA, Gren JA, Baird E. 2020. Exploring the visual world of fossilized and
649   modern fungus gnat eyes (Diptera: Keroplatidae) with X-ray microtomography. *J R Soc*
650   *Interface* **17**. doi:10.1098/rsif.2019.0750
651 Taylor GJ, Tichit P, Schmidt MD, Bodey AJ, Rau C, Baird E. 2019a. Bumblebee visual

652   allometry results in locally improved resolution and globally improved sensitivity. *Elife*
653   **8**. doi:10.7554/eLife.40613
654 Taylor GJ, Tichit P, Schmidt MD, Bodey AJ, Rau C, Baird E. 2019b. Data from: Bumblebee
655   visual allometry results in locally improved resolution and globally improved sensitivity.
656   doi:https://doi.org/10.5061/dryad.23rj4pm
657 Vo NT, Atwood RC, Drakopoulos M. 2018. Superior techniques for eliminating ring artifacts
658   in X-ray micro-tomography. *Opt Express* **26**:28396. doi:10.1364/OE.26.028396
659 Wilby D, Aarts T, Tichit P, Bodey A, Rau C, Taylor G, Baird E. 2019. Using micro-CT
660   techniques to explore the role of sex and hair in the functional morphology of
661   bumblebee (Bombus terrestris) ocelli. *Vision Res* **158**:100–108.
662   doi:10.1016/j.visres.2019.02.008
663